RSC Mechanochemistry

ROYAL SOCIETY OF CHEMISTRY

PAPER

View Article Online
View Journal | View Issue

Check for updates

Cite this: *RSC Mechanochem.*, 2024, **1**, 196

Operando exploration of tribochemical decomposition in synthetic FeS_2 thin film and mineral iron pyrite†

E. Muñoz-Cortés, [a] J. Sánchez-Prieto, [‡b] B. Zabala, [c] C. Sanchez, [ad] E. Flores, [e] A. Flores, [f] E. Roman,[g] J. R. Ares [a] and R. Nevshupa [*h]

Received 4th December 2023
Accepted 10th March 2024

DOI: 10.1039/d3mr00027c

rsc.li/RSCMechanochem

Tribochemical decomposition of thin-film synthetic iron disulfide and mineral iron pyrite was studied using a combination of *operando* mass-spectrometry coupled to ultrahigh vacuum tribochemical cell and the gas expansion system. The composition and kinetics of gas emission were analyzed using an original methodology. It was found that carbon-containing gases were dominating. The sulfur-containing gases comprised H_2S, COS and CS_2. The latter two were unexpected. The emission of these gases was traced back to solid-state chemical reactions kinetically controlled by the precursor concentrations and driven through non-thermal mechanisms, which we tentatively assigned to formation of sulfur radicals.

Open Access Article. Published on 11 March 2024. Downloaded on 2/11/2026 9:14:28 AM.
This article is licensed under a Creative Commons Attribution 3.0 Unported Licence.

1 Introduction

Transition metal sulfides find broad applications in both industrial and biological systems.[1,2] Among these sulfides, FeS_2, also known as iron pyrite, is the most abundant compound in Earth's crust. It is inexpensive, non-toxic,[3] and exhibits significant catalytic and electronic properties, making it suitable for a wide range of applications such as energy conversion and storage,[4–6] photocatalysis,[7] photoelectrochemistry,[8,9] coal and waste treatment[10] and more. The surface chemical structure of pyrite plays a crucial role in its chemistry. Key parameters that control the surface chemistry of pyrite include degrees of sulfur depletion, surface disorder, types and concentrations of crystalline defects, and the presence of adsorbed oxygen, water, and carbon, among others.[11,12] Furthermore, its surface chemistry can be influenced by various factors, including pre-treatment and activation conditions like annealing and UV irradiation.[12,13]

While heating has traditionally been the primary means of activating chemical processes involving FeS_2 as a reactant or catalyst, other forms of energy such as electromagnetic, photonic, and mechanical, alone or in combination, can also be employed for this purpose.[14,15] Mechanochemical activation of pyrite is particularly attractive due to its potential to increase the capacity of chemical processing installations and reduce energy consumption and costs.[16] The advantageous outcomes of mechanochemical processing in terms of enhancing mineral reactivity are ascribed to structural modifications, encompassing the generation of defects, polymorphic alterations, refinement of grains and crystallites, and lattice strain.[17] These changes can even enable thermodynamically unfavourable reaction pathways.[18]

Despite significant research efforts, the mechanistic aspects of mechano- and tribochemically activated heterogeneous catalysis remain elusive.[16,18–21] The main challenge lies in the fact that mechanochemical reactions occur at nearly inaccessible mechanical interfaces, while only a limited number of techniques are available for their *operando* characterization.[22,23] Among these techniques, Mechanically Stimulated Gas Emission Mass Spectrometry (MSGE-MS) has emerged as a powerful method over the last two decades.[24–26] By employing tribological action such as rubbing or scratching, MSGE-MS allows for precise and controlled mechanical activation of materials and coatings on a micrometre to nanometre scale under well-controlled load, speed, and environmental conditions. By

[a]*MIRE-group, Departamento de Física de Materiales, Facultad de Ciencias, Universidad Autónoma de Madrid, Madrid 28049, Spain*
[b]*Centre for Micro Analysis of Materials, Universidad Autónoma de Madrid, C/ Faraday 3, Madrid 28049, Spain*
[c]*Materials and Tribology Unit, Tekniker, C/ I. Goenaga 5, Eibar 20600, Spain*
[d]*Instituto Nicolás Cabrera, Universidad Autónoma de Madrid, Francisco Tomás y Valiente 7, Madrid 28049, Spain*
[e]*Departamento de Física Aplicada, Centro de Investigación y de Estudios Avanzados (CINVESTAV), Merida 97310, Mexico*
[f]*Departamento de Física de Polímeros, Elastómeros y Aplicaciones Energéticas, Instituto de Ciencia y Tecnología de Polímeros (ICTP), CSIC, C/ Juan de la Cierva 3, Madrid 28006, Spain*
[g]*Institute of Materials Science of Madrid (ICMM), CSIC, C/ Sor Juan Inés de la Cruz 3, Madrid 28048, Spain*
[h]*Eduardo Torroja Institute of Construction Sciences (IETCC), CSIC, C/ Serrano Galvache 4, Madrid 28033, Spain. E-mail: r.nevshupa@csic.es*

† Electronic supplementary information (ESI) available: XRD diagrams, RBS and ERDA data with fits, XPS binding energies, assignment of the mass-spectrometry signals to gas ions, ESD *vs.* electron energy, thermal gas desorption data, FTIR of mechanically affected zone, nanoindentation results and the method of calculation of contact temperature. See DOI: https://doi.org/10.1039/d3mr00027c

‡ Present address: Institute for the Structure of Matter, CSIC, Serrano 123, Madrid 28006, Spain.

© 2024 The Author(s). Published by the Royal Society of Chemistry

Open Access Article. Published on 11 March 2024. Downloaded on 2/11/2026 9:14:28 AM. This article is licensed under a Creative Commons Attribution 3.0 Unported Licence.

integrating this technique with mass spectrometry, it becomes possible to accurately detect and quantify volatile products that swiftly propagate in vacuum from buried mechanical interfaces, thereby facilitating the real-time characterization of tribochemical reactions.[27–29] Up to now, mass spectrometry of emitted gases has been successfully employed across various studies, revealing tribochemical processes within diverse materials such as amorphous carbon,[30,31] polymers,[32] metal alloys,[29,33] minerals[34–37] and hydrides.[33,38] In the present study, our focus is on investigating the tribochemical processes on the submicrometre scale in two forms of iron sulfide: natural mineral and synthetic thin film. We employed MSGE-MS to gain a comprehensive understanding of these processes. Given that mechanochemistry is the intersection of chemistry and mechanics, the MSGE-MS research is complemented by a range of surface structural, chemical, mechanical and tribological characterization techniques. When combined, these techniques offer a more profound understanding of the fundamental mechanisms governing mechanically induced chemical processes in both mineral and thin film FeS_2.

2. Materials and methods

2.1 Materials

FeS_2 thin films were obtained by sulfuration of Fe coatings, which were deposited by thermal evaporation of iron powder (Goodfellow, 99.99%) on soda lime glass substrates under high vacuum. The initial thickness of the Fe coatings was 300 ± 20 nm as measured using quartz crystal microbalance. The Fe coating was transferred into a glass ampoule, which contained a small amount of sulfur powder (Merck, 99.99%) placed at one end. The ampoule was evacuated down to 10^{-5} mbar and sealed. Then, sulfur was sublimated by heating to 300 °C for 20 h, while sulfur vapour at a pressure of about 0.065 bar reacted with the Fe film.[39] After sulfuration, the coatings were kept in the same sealed ampoules at room temperature until they were characterized. Natural pyrite was used to contrast the results obtained for artificial FeS_2 thin film. A sheet of iron pyrite was cut from a native crystal proceeding from Peru mines and polished. X-ray diffraction analysis showed a typical cubic crystal structure of the mineral sample (see ESI†).

2.2 Experimental techniques and procedure

The iron coatings' crystal structure was analyzed both before and after sulfuration using grazing-angle X-ray diffraction (XRD). This was accomplished by employing Cu Kα radiation and maintaining a fixed incidence angle of 1.7°. To determine the mean crystallite size, the Scherrer formalism was applied to the main Bragg reflection peak (200). Film thickness measurements were conducted at the film edge utilizing a stylus profilometer, achieving an accuracy of 10 nm.

The mechanical properties of the FeS_2 coatings were investigated through nanoindentation (G200, KLA Corp.), utilizing a Berkovich diamond tip in dynamic contact mode. The maximum indentation depth was 100 nm constrained to remain below 10% of the total coating thickness. The loading cycle was carried out at a constant indentation strain rate of 0.1 s^{-1} and a small oscillating force was superimposed to this loading ramp (75 Hz of frequency, amplitude of 2 nm). Continuous measurement of the contact stiffness[40] was achieved on the basis of the phase lag between the sinusoidal force and the penetration produced.

X-ray Photoemission Spectrometry (XPS) was used to obtain information on chemical state of various elements under ultra-high vacuum (UHV) with a pressure below 10^{-8} Pa. Mg K_α radiation with an energy of 1253.6 eV was employed. The charge correction was done by setting the C 1s (C–C, C–H) peak binding energy to 284.8 eV. To eliminate any airborne adsorbed contaminants from the sample surface, ensuring a pristine surface for subsequent XPS analysis, the samples underwent Ar^+ ion sputtering with an energy of 1 keV and an incident angle of 60° with respect to the sample normal. The sputtering depth was around 1.3 Å. It should be noted that Ar^+ ions for sputtering can potentially alter the chemical oxidation state[41] of Fe and/or S and/or change the surface composition[42] due to preferential sputtering. No additional treatment was performed. High-resolution XPS analysis of Fe 2p, S 2p, O 1s, and C 1s was conducted through the fitting process employing the minimum possible number of components compatible with the expected chemistry. For instance, both the Fe $2p_{3/2}$ and Fe $2p_{1/2}$ spin–orbit peaks were fitted to ensure the coherence of the procedure, while assuming a Shirley background. For the sake of simplicity, only the Fe $2p_{3/2}$ bands are discussed here. The S 2p peak was fitted employing a S $2p_{3/2}$ S $2p_{1/2}$ doublet, considering the theoretical spin–orbit coupling ratio of 1 : 2. A fixed separation of 1.2 eV between the $S_{2p3/2}$ and $S_{2p1/2}$ was maintained based on literature[43] for data processing.

Electron Stimulated Desorption (ESD) coupled with mass spectrometry was used to examine the chemical composition of the adsorbed layers and the surface chemical groups. The sample was bombarded with electrons using an electron gun positioned at a 60° angle to the surface normal. Unless otherwise mentioned, the electron energy used was 600 eV. The ions, which were generated on the surface due to electron bombardment, released from the sample and were detected using a quadrupole mass spectrometer, situated in front of the sample. More details about the setup and process of the ESD experimental system can be found elsewhere.[44]

Thermal Gravimetric analysis of thin films could not be carried out because of the infinitesimal mass of the film in comparison with the mass of the glass substrate. However, the gases emitted during progressive heating under both Ar and dry air flows were analyzed using a mass spectrometer. The rate of linear heating was set at 5, 10, and 20 °C min^{-1}. The emitted gases were analysed in the range of 1–90 a.m.u.

The Rutherford Backscattering Spectrometry (RBS) and Elastic Recoil Detection Analysis (ERDA) techniques, available at the Centre of Micro Analysis of Materials of Autonomous University of Madrid, were employed to determine the elemental composition of the sample surfaces.[45] Its 5 MV linear tandem accelerator facility provides the required ion beams. In this study, a collimated He^+ beam with energies of 3.035 or 4.260 MeV extracted from the accelerator was used, while choice

Open Access Article. Published on 11 March 2024. Downloaded on 2/11/2026 9:14:28 AM. This article is licensed under a Creative Commons Attribution 3.0 Unported Licence.

of these energies' values justified under resonant conditions for oxygen and carbon respectively. For RBS analysis, the backscattered ions were detected at an angle of 170° to the direction of the incident ion beam. In the case of ERDA, the ions were directed to the surface at an incident angle of 75° to the surface normal. Recoiled particles were collected at 30°. To filter out heavier ions, a 19 μm thick mylar film was placed in front of the detector to obtain the hydrogen depth profile. The total ion dose in each measurement was set to 15 μC with a particle flux of 5.5 $\times 10^{12}$ cm^{-2} s^{-1} and a probe size of 1.5 × 1.5 mm^2. The spectra were taken with the samples at random orientations. For energy-to-depth conversion, common SRIM (Stopping and Range of Ions in Matter) energy loss data were used, along with reference samples of MgH_2 Er-doped TiO_2 coatings. The RBS-ERDA spectra were fitted using SIMNRA simulation software.

The gases emitted during mechanical activation of the materials were analysed using an original UHV experimental system equipped with a quadrupole mass spectrometer (Hiden HALO), a reciprocating motion UHV-grade friction cell, and a dynamic gas expansion system (Fig. 1). Such a configuration allows accurate quantification of minute emission rates down to 1 pmol s^{-1}. The samples were rubbed under UHV using alumina spheres, 3 mm in diameter. The rubbing conditions, unless otherwise stated, were as follows: the normal load of 0.44 N, the frequency of reciprocating motion of 1 s^{-1}, and the mean rubbing velocity of 0.18 m s^{-1}. The experimental system is schematically shown in Fig. 1 and described in detail elsewhere.[24,25] Before the tests, the alumina spheres were thoroughly degreased consecutively in acetone and isopropanol ultrasonic baths. After drying, they were submerged in a hot Piranha solution to remove carbon and metal residues, rinsed with ultrapure water, and dried in an N_2 stream. The differential mass spectra (DMS) were derived by subtracting the mean steady background mass spectra from the mean mass spectra recorded during the application of the mechanical stimulus.[46,47] Only statistically significant changes ($\alpha = 0.05$) in DMS were analysed among the channels within the 1–100 a.m.u. range. To ensure comparability, the mass spectra were normalized by dividing by the total ion current in each spectrum. The tentative identification of ion species was based on reference cracking patterns from the NIST Webbook. The gas composition was determined through a backward stepwise regression method, in which we utilized reference mass spectra of various potential gas precursors. These spectra were fitted in various combinations to the experimental DMS with the aim of identifying the combination that included the fewest precursors and achieved a high R_{adj}^2 value. Behavioural analysis (BA)[47,48] was employed to develop better understanding of the mechanisms of underlying tribochemical processes. BA allows to exploration of the short- and long-term trends of highly dynamic emission time series, to establish the degree of correlation between the mass spectrometer signals, and to trace them back to the possible emission sources in the mechanically affected bulk material and/or on the mechanically affected surfaces.

Chemical changes in the Mechanically Affected Zones (MAZ) were studied using vibrational spectroscopy (Raman and FTIR). All the results were benchmarked against the spectra obtained from neighbouring pristine surfaces. Raman spectra were measured using a 532 nm laser in air. Infrared micro-reflectance spectra were obtained using a micro-FTIR spectrometer.

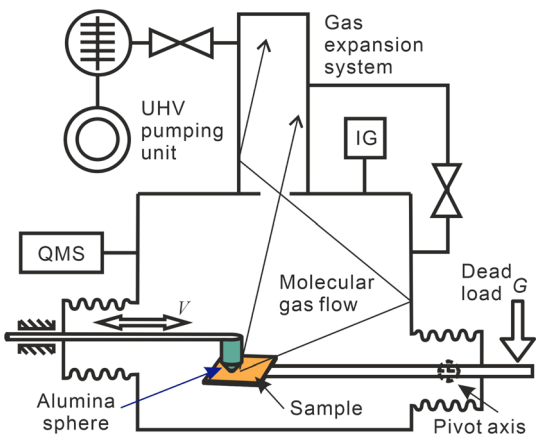

Fig. 1 Schematic drawing of the experimental system for study of chemical reactions through the mass-spectrometric analysis of emitted gases. IG – ion gauge for total pressure measurements, QMS – quadrupole mass spectrometer.

3. Results

3.1. Structure, composition and chemical properties

Based on profilometer measurements,[49,50] the thickness of the FeS_2 film ranged from 1000 to 1100 nm depending on the lot. This value is 3.3–3.7 times larger than the initial Fe film's thickness. This augmentation corresponds to the 3.3-fold increase in molar volume ratio between Fe and FeS_2. The XRD pattern of the FeS_2 thin films displayed an identical pattern to that of a powder pyrite standard (PDF 01-071-0053), confirming the presence of a pyrite crystal structure. No other crystallographic phases and no signal from the original Fe film were detected, indicating the complete conversion of the iron coating to iron sulfide (see Fig. S1 and S2 in the ESI†). Furthermore, no crystallographic texture was observed in the films, suggesting a random orientation of the crystallites. The mean crystallite size of the sulfurated iron films was determined to be approximately 21 nm, which is consistent with the data reported in previous studies.[49,50]

The depth profiles of elemental concentrations are shown in Fig. 2. The measured ERDA and RBS spectra and the corresponding fitting results are presented in ESI (Fig. S4–S9†). Natural pyrite exhibited a surface layer with a thickness of less than 500 nm, which was enriched with oxygen and carbon. There was an elevated concentration of hydrogen at the very top of this layer, which decreased sharply with increasing depth but remained at approximately 2 at% down to several micrometres. The sulfur-to-iron (S/Fe) ratio closely matched the stoichiometric value throughout the depth profile.

In contrast, the elemental distribution in the FeS_2 film was notably more complex. The surface layer was thinner than that in natural pyrite and had a significantly higher oxygen

© 2024 The Author(s). Published by the Royal Society of Chemistry

Open Access Article. Published on 11 March 2024. Downloaded on 2/11/2026 9:14:28 AM.
This article is licensed under a Creative Commons Attribution 3.0 Unported Licence.

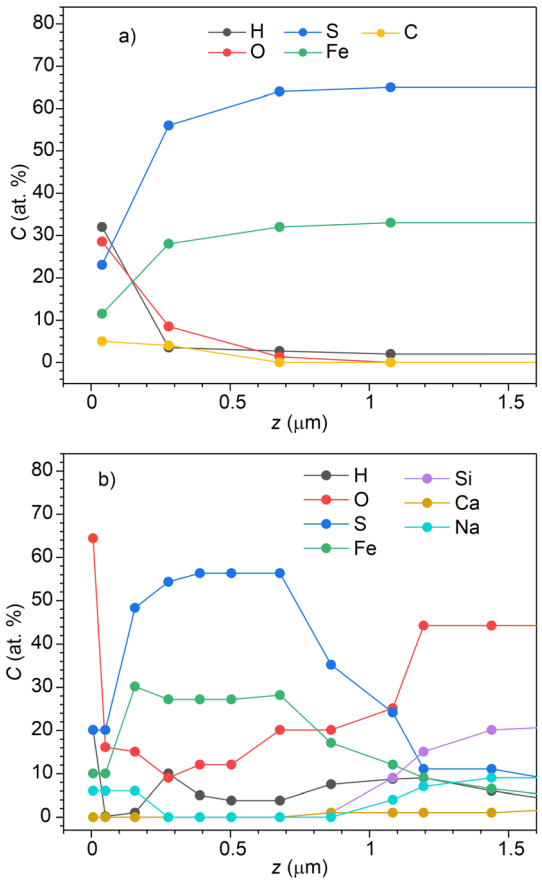

Fig. 2 Depth profiles of elemental concentrations for (a) natural pyrite and (b) FeS_2 thin film.

concentration. As the depth increased, the concentration of oxygen decreased but did not completely vanish. Within the depth range of 500–700 nm, it reached a minimum of around 3 at% and then gradually increased with depth. Sodium and calcium exhibited a similar increase in concentration, likely due to the diffusion of these elements from the soda-lime substrate into the coating during thermal sulfuration.

Interestingly, a hydrogen peak of around 12 at% was observed at a depth of approximately 300 nm, with another broader hydrogen peak located near the interface of the film with the substrate. This latter peak could be attributed to hydroxyl groups that remained on the glass surface. Carbon was undetectable, even under C-resonance experimental conditions. The S/Fe ratio ranged from 1.5 to 1.7 within the depth range of 0 to 500 nm and approached 2 at the deeper regions of the coating.

Table 1 displays the elemental surface composition of both the thin films and the natural FeS_2 mineral, acquired through energy-dispersive X-ray analysis (EDX).

The XPS spectrum of the pristine sample indicates the presence of Fe and S, as well as notable quantities of C, O, and Na. Carbon and oxygen are typical in materials that have been exposed to the atmosphere, as they can originate from airborne pollutants or reactions with atmospheric gases. The presence of Na is consistent with prior studies.[50,51] Following sputtering, the

Table 1 Surface elemental composition (mean value ± interval of variation) of FeS_2 thin-film and mineral samples

	Mineral pyrite	Thin film
Method	EDX	EDX
Fe	26.0 ± 2	31.4 ± 1.25
S	54.0 ± 4	65.6 ± 2.5
O	8.0 ± 2	0.89 ± 0.85
Na		0.42 ± 0.3
Ca		0.30 ± 0.1
Si	0.04 ± 0.04	1.79 ± 0.29
Cr	0.1 ± 0.1	
S/Fe ratio	2.08 ± 0.22	2.09 ± 0.12

carbon concentration decreased by almost two-fold, while the sodium concentration increased 2.4 times (see Fig. S11 in ESI†). These observations imply the presence of a very thin carbon layer on the surface, likely originating from the condensation or adsorption of airborne impurities. In contrast, Na must be distributed within the bulk rather than on the surface, aligning with the hypothesis of Na diffusion from the substrate.[50,52]

In the fine Fe 2p XPS spectra (Fig. 3a), two prominent bands are evident at 706.7 eV (designated as Fe1) and 719.5 eV, corresponding to the binding energies of Fe $2p_{3/2}$ and Fe $2p_{1/2}$,

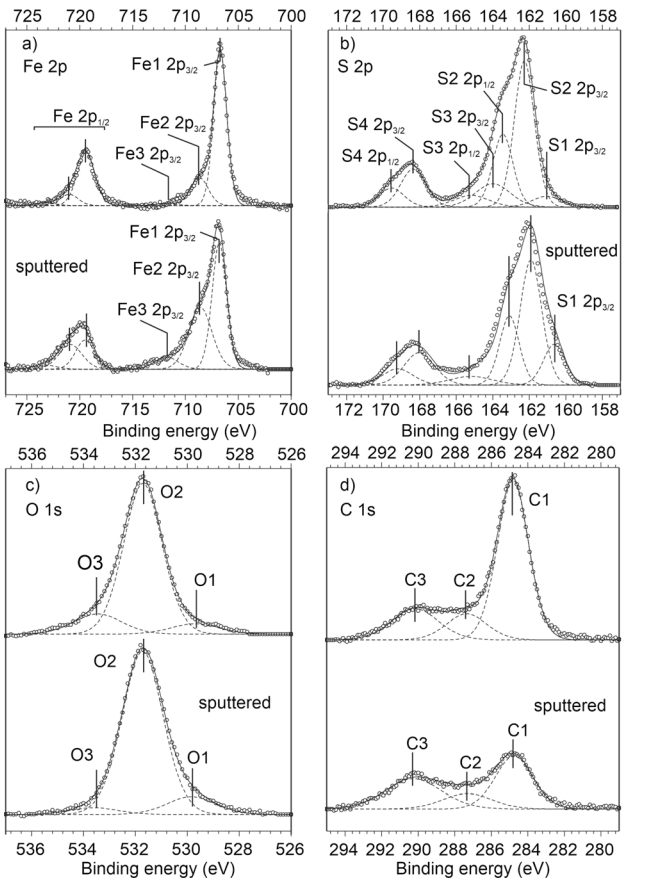

Fig. 3 XPS fine spectra and deconvolutions: (a) Fe 2p; (b) S 2p; (c) O 1s; (d) C 1s.

Open Access Article. Published on 11 March 2024. Downloaded on 2/11/2026 9:14:28 AM. This article is licensed under a Creative Commons Attribution 3.0 Unported Licence.

respectively. These multiplet splitting bands are indicative of low symmetry Fe^{2+} states in pyrite such as those found on corners, edges, and surfaces.[50,53,54] This supports the hypothesis that the thin-film sample has a highly defective structure. This conclusion is further supported by the RBS results, which revealed a significant concentration of foreign elements like Na, C, and O, as well as the broadened XRD peaks (Fig. S1 in ESI†). Notably, a tail extending from the Fe $2p_{3/2}$ transition into higher binding energies is observed, likely representing iron ions in a more oxidized environment, *i.e.* Fe^{3+}–S or multielectron processes.[55] To achieve a better fit, we introduced two minor components at 708.7 eV (referred to as Fe2) and 711.8 eV (referred to as Fe3). These energy values are consistent with those found in the literature for FeO/Fe_3O_4 and the oxy-hydroxide Fe(OOH).[52] After Ar^+ etching, the Fe 2p spectrum exhibits broadening, but no shift in the maxima's positions was noted. Changes in the relative area contributions can be observed in Table 2. The most significant finding is the relative increase of iron oxides. This suggests that these oxides were not formed during transfer of the samples from the ampoule to the XPS systems, but must be related with the previous steps of the coating deposition or diffusion of oxygen or oxygen-containing groups (OH, CO, *etc.*) from the substrate.

The deconvolution of C 1s spectra (Fig. 3d) resulted in three components centred at 284.8 eV (C1), 285.8 eV (C2), and 288.5 eV (C3). These correspond to C–C/C–H, C–O/C–OH, and HO–C=O groups, respectively.[43,56] Importantly, sputtering led to a significant reduction in the overall carbon content, with a particular decrease in the C1 component, which is likely associated with the surface-adsorbed layer of airborne contaminants. This discovery is consistent with the outcomes of RBS.

Concerning the S 2p peak (Fig. 3b), the relative increase in the FeS (S1 component) can be attributed to the generation of S vacancies during sputtering process. The other constituents of the S 2p band were not notably influenced by sputtering. Fig. 3c illustrates the O 1s spectrum, which underwent deconvolution into three components labelled as O1, O2, and O3, centred at 529.6 eV, 531.6 eV, and 533.6 eV, respectively. The dominating component (O2) was ascribed to OH^- and CO surface groups. Remarkably, sputtering did not induce any noticeable change in the spectrum. The spectra of both Fe 2p and S 2p obtained for sputtered thin-film samples were similar to the corresponding spectra of freshly fractured and oxidized mineral pyrite, in line with literature.[55,57,58]

3.2. Electron-stimulated desorption (ESD)

The ESD mass-spectrum of adsorbed species on FeS_2 thin film is shown in Fig. 4. The two strong components at *m*/*z* 1 and 19 correspond to H^+ and F^+ which are common contaminants encountered in surface studies.[59] Peaks at *m*/*z* 16, 23, 32, and 39 were attributed to O^+, Na^+, S^+ and K^+, respectively. The presence

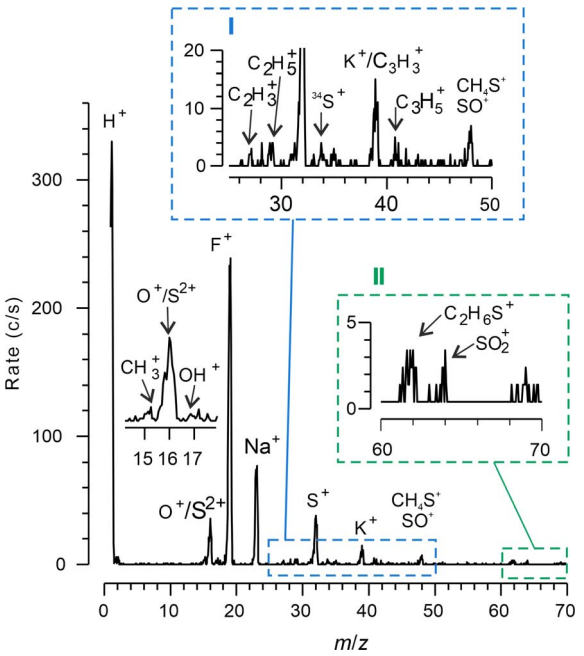

Fig. 4 Mass spectrum of the ions emitted form a thin-film FeS_2 surface and produced through surface ionization by incident electrons at 600 eV.

Table 2 Deconvolution of the XPS spectra

		Area (%)		
Component	Binding energy (eV)	Pristine	Sputtered	Group assignment
Fe1	706.7	78.5	49.8	FeS_2
Fe2	708.7	18.6	42.1	FeO/Fe_3O_4
Fe3	711.8	2.90	8.10	Fe(OOH)
S1	160.8	5.70	16.2	S^{2-} (FeS, sputtering defects)
S2	162.1	61.4	51.3	S_2^{2-} (bulk FeS_2)
S3	164.0	14.0	13.5	S^0 (polysulfide)
S4	168.2	18.9	19.0	SO_4^{2-}, C–SO_3–H/C–SO_3–Na
O1	529.7	7.0	11.0	O^{2-} (iron oxides)
O2	531.7	79.7	84.8	C–O, OH^- ($Fe(OH)_2$, Fe(OOH), *etc.*), carbonates
O3	533.4	13.3	4.2	H–C–O, H_2O (ad.)
C1	284.8	66.5	44.6	C–C, C–H
C2	287.3	14.1	17.0	C=O
C3	290.2	19.4	38.4	Carbonate $(CO_3)^{2-}$

© 2024 The Author(s). Published by the Royal Society of Chemistry

Open Access Article. Published on 11 March 2024. Downloaded on 2/11/2026 9:14:28 AM.
This article is licensed under a Creative Commons Attribution 3.0 Unported Licence.

of alkali metal ions is unsurprising, given their abundance in the soda-lime glass substrate and their high diffusivity at the temperature of thermal sulfuration (300 °C) utilized in this study. Similar findings have been reported previously.[50] Upon closer examination of the regions labelled I and II, various peaks were identified and attributed to C2 and C3 hydrocarbons, hydrogen sulfide and sulfur oxides. Notably, there were no ions at m/z 60 (COS^+). This indicates that, unlike the desorption of H_2S or hydrocarbons, the mechanically induced emission of COS did not involve the desorption of existing surface groups. Instead, it suggests that COS was generated through tribochemical synthesis from some precursors. Consequently, the peak at m/z 62 cannot be assigned to isotopologue $CO^{34}S$, but rather to alkyl thiols or thioethers, consistent with the MSGE mass spectra (see Section 3.4). The absence of peaks at m/z 28 (CO^+), 44 (CS^+/CO_2^+) and 76 (CS_2^+) in ESD spectra suggests that these species were not present on the sample surface before rubbing, but were formed in tribochemical reactions.

The threshold electron energies required for the emission of O^+, S^+ and SO^+/CH_4S^+ determined using an acceleration potential ramp. The measured values, falling within the range of 220 to 280 eV (refer to Fig. S12 in ESI†), were notably higher than the thresholds for electron-stimulated desorption of gases adsorbed on solid surfaces.[56,59,60] In contrast, these values closely resembled the excitation energy of S 2s.[61] This suggest that the fragmentation likely originates from core ionization of the surface groups, followed by subsequent Auger decay of the initial core hole.[44,61]

3.3. Mechanical properties

For mineral pyrite, the elastic modulus, E, displayed a gradual increase at very shallow penetration depths. At a depth of approximately 40 nm, E stabilized at 340 ± 40 GPa (see Fig. S17 in ESI†). This value aligns the results obtained through nanoindentation on monocrystalline pyrite (ranging from 250 to 380 GPa depending on crystal orientation)[62] and the value of 310 GPa obtained *via* ultrasonic measurements on polycrystalline pyrite.[63] Hardness exhibited a similar trend, reaching a stable mean value of $H = 19 \pm 2$ GPa at depths greater than 40 nm. This value is in close agreement with reported data, which state $H = 18 \pm 1$ GPa.[64] The gradual trend observed at depths below 40 nm could be linked to the presence of a surface layer rich in carbon, oxygen, and hydrogen, as identified through Rutherford Backscattering Spectrometry.

In the case of thin-film FeS_2, a similar increasing trend in elastic modulus was observed at depths below 40 nm, reaching a maximum value of around 240 GPa. However, at greater depths, elastic modulus gradually decreased, reaching 184 GPa at a depth of 106 nm, despite maintaining the penetration depth below the recommended 10% of the film thickness. The observed decrease in elastic modulus with depth can be attributed to several factors, including the modulus mismatch between the stiffer FeS_2 film and the more compliant soda-lime glass substrate, the diffusion of Na and other foreign elements from the substrate into the coating during thermal sulfuration, and the presence of micro- and nanopores within the coating, as suggested by the weak nitrogen peak in RBS spectrum (Fig. S10 in ESI†). The higher value for the mineral sample can be attributed to its higher purity and more compact and ordered crystal structure.

3.4. Thermal gas desorption

The primary components of the mass spectra of gases emitted under linear heating of thin-film samples (Fig. 5) were m/z 48 and 64 assigned to SO^+ and SO_2^+, respectively. The mean ratio between them was calculated as $a_{48/64} = 0.563$ (se 0.005). This value is not significantly different from the reference fragmentation coefficient $a_{r,48/64} = 0.493$ for SO_2. When subjected to an argon (Ar) flow, the emission of SO_2 occurred in two distinct events, one around 360 °C and another around 487 °C. The latter peak exhibited a shoulder in the temperature range of 498–524 °C. Both of these desorption events were accompanied by simultaneous decreases in the signal at m/z 32, which can be attributed to the consumption of O_2 residuals present in the Ar gas. No significant desorption or adsorption events were observed for other signals.

Kissinger equation[65] was used to determine the apparent activation energies for desorption, $E_{a,d}$, of SO_2 in the two events by analyzing the slope, a_s, of linear fit of the plot $\ln(\beta/T_m^2) = a_s T_m^{-1} + b$ where β is the heating rate, T_m is the temperature at the peak maximum, and b is the constant[66] (see the inset in Fig. 5a). The $E_{a,d}$ were found to be 60.3 kJ mol^{-1} for the low-temperature event and 102.6 kJ mol^{-1} for the high-temperature event. These values are close to the activation energy values reported for the combustion of iron sulfide concentrates and the oxidation of pyrite.[67–69] It is important to note that the emission of SO_2 from thin film occurred at higher temperatures compared to elemental sulfur (as shown in Fig. S14a in ESI†). The results of thermal degradation of pyrite under dry airflow are presented in Fig. S14 in ESI.†

It can be concluded that the thermal degradation of the FeS_2 thin film primarily takes place through an oxidative mechanism

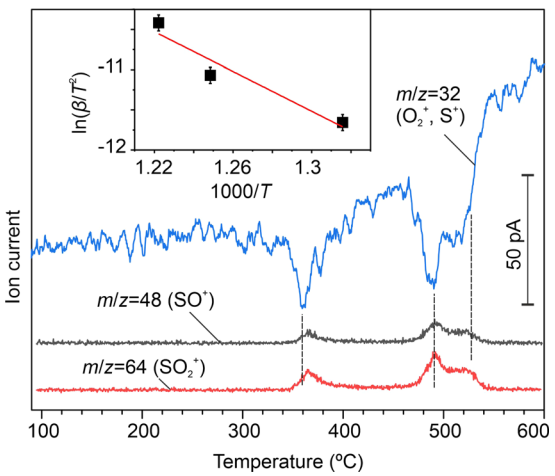

Fig. 5 Variations of mass spectrometer signals during heating thin-film FeS_2 samples under Ar flow, heating rate 5 °C min^{-1}.

Open Access Article. Published on 11 March 2024. Downloaded on 2/11/2026 9:14:28 AM.
This article is licensed under a Creative Commons Attribution 3.0 Unported Licence.

at temperatures exceeding 320 °C. This process leads to the generation of carbon-containing gases, mainly CO_2, and to a lesser extent, C3 hydrocarbons. Notably, there were no observed reactions between carbon and sulfur during heating up to 600 °C. These findings align well with prior investigations into the thermal decomposition of pyrite[68,70,71] and with our results on thermal oxidation (see Fig. S13 and S14 in ESI†).

3.5. Gas emission induced by mechanical activation

The differential mass spectrum (DMS) shown in Fig. 6a illustrates the increase in ion currents, denoted as ΔI, induced by mechanical action.

The signal observed at m/z 2 was unequivocally attributed to H_2^+ ions. Ions at m/z 13–15 were identified as stemming from the fragmentation of methyl groups and methane. However, the signal at m/z 16 appeared notably more intense than would be expected from methane alone. To quantify this, we calculated the empirical fragmentation coefficient for CH_3^+ $a_{15/16} = 0.219$, se = 0.149, defined as the ratio of ion currents between signals I_{15}/I_{16}.[46,72] The $a_{15/16}$ was four-fold smaller than the reference fragmentation coefficient for methane $a_{r,15/16} = 0.888$.[46] This suggests the presence of more than one precursor for ions at m/z 16. Among these, O^+ was the most likely candidate, while S^{2+} was ruled out due to its negligibly small low-energy electron-impact ionization cross-section.[73] O^+ could be formed through the fragmentation of oxygen-containing molecules like CO, CO_2, and COS, whose existence was inferred from signals at m/z 28, 44 and 60, respectively.

In addition, the difference between the empirical and reference fragmentation coefficients for ions at m/z 33 and 34 was not statistically significant ($a_{33/34} = 0.390$, se = 0.153, $a_{r,33/34} = 0.420$, p-value 0.841, and df = 76). Therefore, the signals at m/z 33 and 34 were unequivocally assigned to hydrogen sulfide (H_2S). However, the signal at m/z 32, corresponding to S^+, was significantly disproportionate ($a_{32/34} = 4.69 \pm 1.64 \gg a_{r,32/34}(H_2S) = 0.444$), most likely, due to the contribution of other sulfur-containing gases. The ratio of $CO^{34}S$ to the sum $CO^{32}S$ + $CO^{34}S$ ($I(m/z\ 62)/(I(m/z\ 62) + I(m/z\ 60)) = 0.0445$, se = 0.037) aligned with the natural relative abundance of the ^{34}S isotope: 0.0396–0.0477.[74] Consequently, we attributed the ions m/z 60 and m/z 62 to $CO^{32}S^+$ and $CO^{34}S^+$, respectively. However, it's essential to acknowledge that the presence of unidentified alkyl sulfides, thiols, or other compounds cannot be entirely ruled out. Finally, the two weak components at m/z 64 and 76 were attributed to SO_2^+/S_2^+ and CS_2^+, correspondingly.

The DMS for mineral pyrite was not significantly different (Fig. 6b) from that of thin film except some new, weak components at m/z 26–30, 39 and 41 likely originating from C2 and C3 alkanes. Notably, the components at m/z 14–16 were more pronounced compared to the thin-film FeS_2 and closely matched the reference mass spectrum of methane ($a_{15/16} = 0.93$, se = 0.182, $a_{r,15/16} = 0.888$, p-value 0.954, df = 30; $a_{14/16} = 0.184$, se = 0.024, $a_{r,14/16} = 0.204$, p-value 0.834, df 30).

Additional insights into the potential precursors of the mass spectrometer signals were obtained by analysing the correlations and behavioural features of their time series. Fig. 7 presents Spearman's rank correlation coefficients between the mass spectrometer signals. For thin films, robust correlations between m/z 16, 28, 44, and 60 indicate that the corresponding oxygen-containing gases are emitted coherently and likely originate from the same precursors or stem from the same tribochemical reaction.

The correlation between ion fragments associated with H_2S was somewhat weaker. For mineral FeS_2, the strong correlation

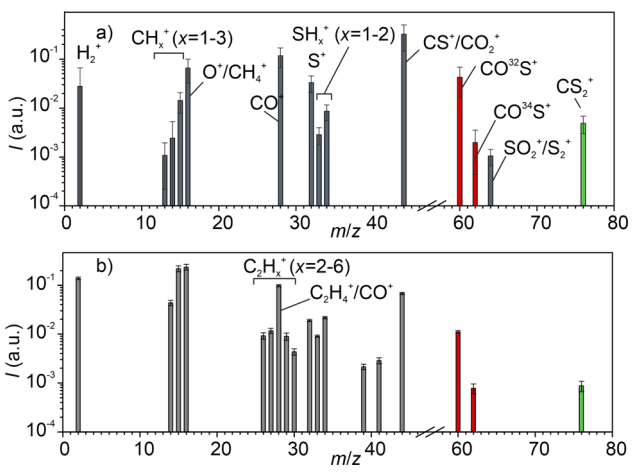

Fig. 6 Mean differential mass spectra of gases, which were emitted under vacuum due to rubbing of (a) FeS_2 thin films and (b) mineral iron pyrite. Standard errors of the mean are shown by vertical lines.

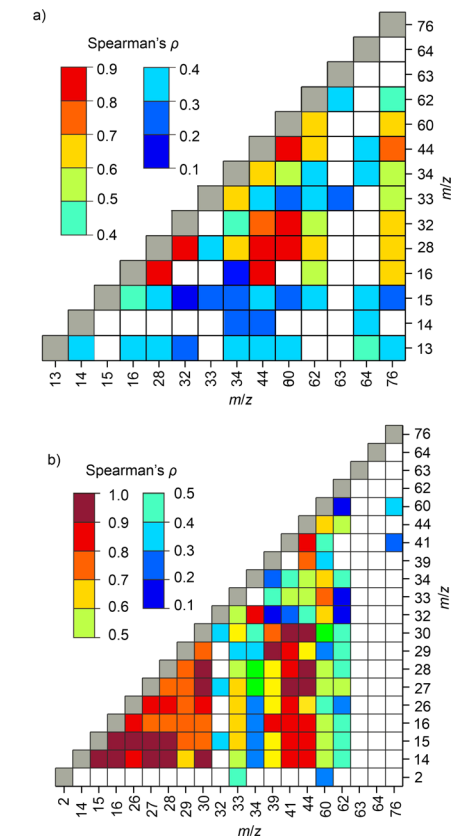

Fig. 7 Spearman's rank correlation coefficients: (a) thin film, (b) mineral.

© 2024 The Author(s). Published by the Royal Society of Chemistry

Open Access Article. Published on 11 March 2024. Downloaded on 2/11/2026 9:14:28 AM.
This article is licensed under a Creative Commons Attribution 3.0 Unported Licence.

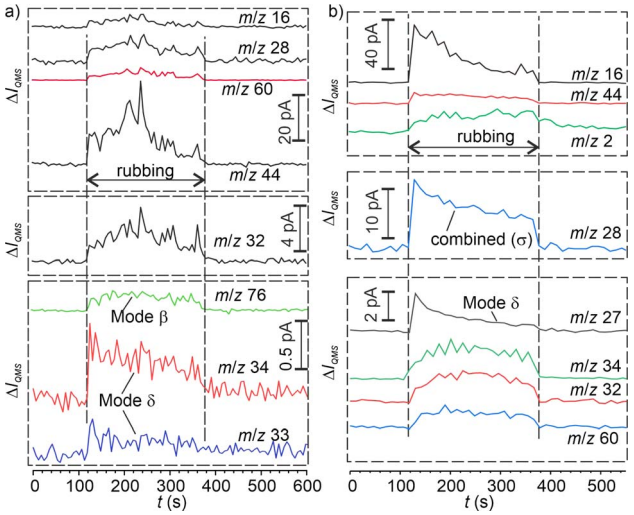

Fig. 8 Time series of mass spectrometry signals: (a) FeS_2 thin-film, (b) mineral pyrite.

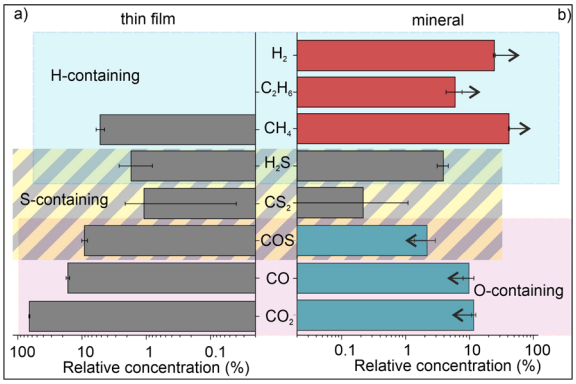

Fig. 9 Relative compositions of gases emitted from (a) thin film FeS_2 and (b) mineral pyrite under mechanical solicitation. Blue region represents H-containing gases, purple region represents O-containing gases, and hatched region represents S-containing gases. The corresponding blue and red bars in the graph of mineral pyrite highlight the specific components that exhibit increased or decreased levels compared to the thin-film sample.

between *m*/*z* 14–15, 26–28 and 41 supports their assignment to saturated aliphatic hydrocarbons. Furthermore, the robust correlation between *m*/*z* 44 with *m*/*z* 16, 27, 28, 30, 39 and 41 suggests that the former is primarily associated with C3 hydrocarbons rather than CO_2. The signal at *m*/*z* 32 (S^+) correlated mainly with *m*/*z* 34 (H_2S^+) and, to a lesser extent, with *m*/*z* 60 (COS^+), reinforcing the conclusion that H_2S and COS are the primary sulfur-containing gases emitted. It's worth noting that *m*/*z* 64 associated with S_2^+/SO_2^+ didn't exhibit significant correlations with any other signals, indicating entirely different chemical reactions responsible for these components' emission. Interestingly, for both samples, *m*/*z* 76, assigned to CS_2^+, displayed a moderate correlation with oxygen-containing ions, implying that CS_2 and COS can be produced from the same carbon-containing precursors through competitive reactions. The behavioural patterns of mass-spectrometric signals were identified and labelled as modes β, δ, and σ following established classification criteria.[47] Some examples of these patterns are illustrated in Fig. 8, while Table 3 summarizes their assignment to the signals. Mode β is characterized by a nearly rectangular or slightly humped profile, often accompanied by a series of random transitory emission events (RTEEs). Following the cessation of rubbing, a rapid decline was typically observed in this mode. Mode δ displayed a triangular or trapezoidal profile with a sharp initial spike at the onset of rubbing, followed by a gradual decrease, and an insignificant contribution from RTEEs. Mode σ represents a combination of modes β and δ. This mode appears when ions of the same mass, but originating from various gas precursors, coexist, for example, CO^+ and $C_2H_4^+$ both contributing to *m*/*z* 28. Table 3 illustrates that in the case of the thin film, mode δ is primarily associated with H_2S, while in the case of mineral pyrite, it corresponds to C1–C3 hydrocarbons.[46] On the other hand, mode β is characteristic of H_2, O-containing gases and CS_2 in both cases. Notably, in the case of thin film, methane and H_2S followed mode β instead of mode δ, which is observed for mineral pyrite. The resulting combinations of possible gas precursors that best explain the DMS are illustrated in Fig. 9. Notably, the compositions of gases were quite similar for both samples, except for the absence of ethane and hydrogen in the case of the thin film, but the relative contributions of the components were different. In the thin film, oxygen-containing gases dominated, with CO_2, CO, and COS accounting for 92% of the total. On the other hand, mineral pyrite exhibited a prevalence of hydrogen and hydrocarbons, making up 66% of the total. The relative concentration of S-containing gases was similar for both samples. These findings align with the elemental composition of the samples determined using XPS, RBS and ERDA. This will be further discussed in Section 4.

Table 3 Classification of mass-spectrometry components according to behaviour mode of their time series

Behaviour of time series	Thin film	Mineral
Mode β	2, 14–16, 28, 32, 44, 60, 62, 64, 76	2, 28, 32–34, 44, 60, 62, 76
Mode δ	33, 34	14–16, 26, 27, 29, 30, 39, 41
Combined (σ)	—	28

3.6. Characterization of mechanically affected surface zones

The microscopy images of worn areas, as depicted in Fig. 10, along with the profilometry data presented in Fig. 11, illustrate a gradual wearing of the coating as the number of cycles of the indenter's reciprocating motion increases. The coating exhibited good adhesion to a substrate – spalling becomes apparent only after a higher number of cycles. After 1500 cycles, the coating wore down completely, revealing the underlying substrate. The characteristics and distribution of the wear debris on the sides of the Mechanically Affected Zone (MAZ) and

Open Access Article. Published on 11 March 2024. Downloaded on 2/11/2026 9:14:28 AM.
This article is licensed under a Creative Commons Attribution 3.0 Unported Licence.

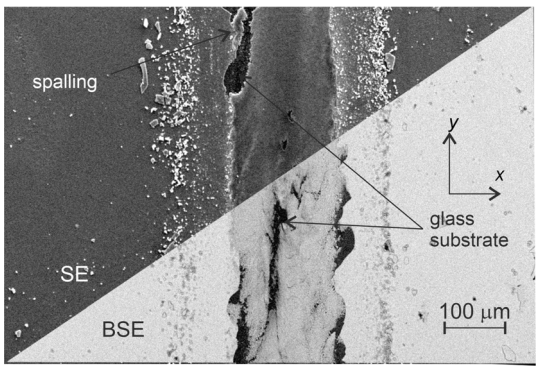

Fig. 10 A combined image of backscattered (BSE) and secondary (SE) electrons of a portion of the mechanically affected zone.

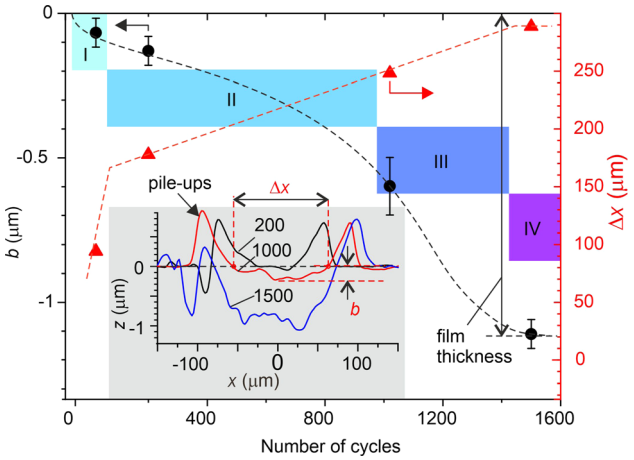

Fig. 11 Geometric characteristics of the worn zones: mean depth, Δz, and mean width Δx as a function of the number of mechanical activation cycles. Dashed lines serve as visual guides. (Inset) representative cross-sectional profiles of worn zones (sliding direction along y) after 200, 1000 and 1500 cycles. Rectangles schematically illustrate wear stages: (I) run-in stage; (II) steady wear; (III) catastrophic wear of the coating and intensive spalling; (IV) substrate wear.

at its edges suggest an abrasive type of wear for the coating. The S/Fe ratio measured on the MAZ was not different from the pristine surface. However, various wear debris in the central part of MAZ showed the S/Fe below the stochiometric one: 1.2–1.6. Sulfur depletion in the debris could be due to emission of sulfur-containing gases. Micro-Raman spectroscopy of the pristine surface showed three prominent peaks at 341 cm^{-1}, 377 cm^{-1}, and 426 cm^{-1}, which have been identified as the E_g (S_2 dumbbell stretch), A_g (S–S vibration bands stretch), and T_g (a combination of stretch and vibrational signal) symmetric vibrational modes, respectively[75–78] (refer to Fig. 12). Notable changes in Raman spectra were observed both in the MAZ and on wear debris. The E_g and A_g bands experienced blueshift, while the T_g band disappeared. Furthermore, two new bands associated with hematite (α-Fe_2O_3) appeared at 276 cm^{-1} and 216 cm^{-1}. Additionally, in the MAZ, the Raman peaks corresponding to FeS_2 exhibited broadening indicating a decrease in the degree of crystallinity.

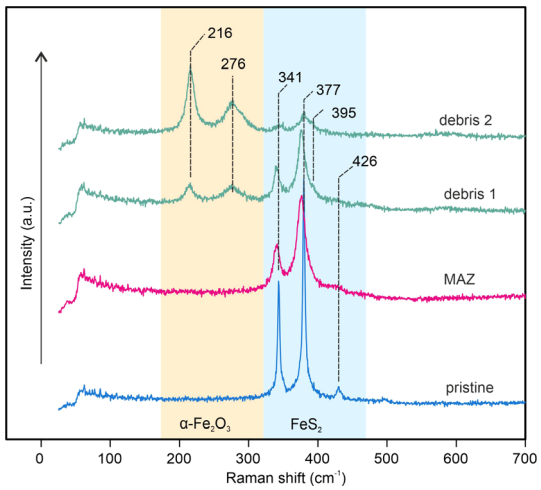

Fig. 12 Micro-Raman spectra measured on pristine zone, mechanically affected zone (MAZ) and wear debris.

3.7. Thermal effect of friction

The "flash" temperature, which represents the instantaneous surface temperature increase at the sliding interface, was calculated using Jaeger's solution for a localized moving heat source.[79,80] The description of the model is provided in ESI.† Several input parameters necessary for the model were determined experimentally. For instance, the friction coefficient between a 3 mm diameter steel sphere and the FeS_2 thin film was determined in a separate test. This test was conducted under high vacuum conditions with a normal load of 2.04 N. The details of the vacuum tribometer used for this experiment and the specific experimental conditions are available in a separate ref. 25. The parameters used for the calculation and the results are provided in Table 4. The calculated "flash" contact temperature (the ambient temperature plus the temperature increase) of approximately 305 K falls significantly below the thresholds for both thermal decomposition and thermal oxidation of pyrite (see Section 4), suggesting the involvement of distinct tribochemical processes in gas emission.

4. Discussion

The surprising result of this study, is the observation of CS_2 and COS emission when thin film and mineral pyrite underwent mechanical activation at room temperature. Under an inert atmosphere (N_2, He or vacuum) thermal decomposition of pyrites starts above 873 K[87] and proceeds through a multi-step process in the sequence of pyrite → pyrrhotite → iron, *i.e.* through a gradual loss and evaporation of sulfur.[70] The process stops when sulfur concentration in the mineral reaches an equilibrium value depending on the pressure of sulfur gas and temperature. Reduction with hydrogen occurs at around 773 K. As the temperature gradually increased from 673 to 1073 K under H_2–CO gas mixture[91] the predominant gaseous products shifted on the following order: COS → S → H_2S → S_2 → CS_2.

© 2024 The Author(s). Published by the Royal Society of Chemistry

Open Access Article. Published on 11 March 2024. Downloaded on 2/11/2026 9:14:28 AM.
This article is licensed under a Creative Commons Attribution 3.0 Unported Licence.

Table 4 The parameters used in the calculation of the "flash" temperature, along with the calculated results

		FeS_2		
	Units	This study	Literature	Al_2O_3
Hardness	MPa		60–100 (ref. 64, 81–83)	1800
Young modulus	GPa	170 ± 50	310 (ref. 63)	345 (ref. 84 and 85)
Poisson's ratio			0.15–0.29 (ref. 86 and 87)	0.23 (ref. 85 and 88)
Thermal conductivity	$W\ m^{-1}\ K^{-1}$		45.5 (ref. 89)	34 (ref. 71)
Density	$kg\ m^{-3}$		5020 (ref. 90)	3780
Heat capacity	$J\ kg^{-1}\ K^{-1}$		62.6 (ref. 71)	784
Max. temperature increase ΔT (K)			9.1 (at 0.33 N load)	

Under oxidative environments, pyrite remains stable up to 673 K,[70,83,87] while the emitted gas was usually SO_2.[89] In oxygen-containing atmospheres the transformation of pyrite can take place in two different ways depending on the temperature and oxygen concentration. Below *ca.* 800 K and higher oxygen concentrations, pyrite will be directly oxidized. At higher temperatures or low oxygen pressure pyrite will be transformed by a two-step process: the thermal decomposition to form porous pyrrhotite as the first step, and the successive oxidation of the formed pyrrhotite as the second step.[70] Thermal oxidation of pyrite is a highly complicated process occurring through no less than 16 concurrent reactions.[68] The main process leads to the formation of hematite and sulfur dioxide through reaction (R1).[70] Ferrous and ferric sulfates can also form as minor products. Thermal decomposition of pyrite is described by the reaction (R2),[70,92] in which subscript "ad" stands for adsorbed states. Its activation energy is only 30 kJ mol^{-1}.[93] However, the apparent activation energy for thermal decomposition is much higher, 96–310 kJ mol^{-1}, because it involves the diffusion of sulfur atoms and the recombinative molecular desorption of S_2, with activation energies of 90 and 200 kJ mol^{-1}, respectively. Pyrrhotite formed in R2 can be further decomposed following the reaction (R3)

$$FeS_2 + \frac{11}{2}O_2 \rightarrow Fe_2O_3 + 4SO_2 \quad (R1)$$

$$FeS_2 \rightarrow FeS + \frac{1}{n}S_n \quad (R2)$$

$$FeS_x \rightarrow Fe + xS_{ad} \quad (R3)$$

$$FeS_2 + H_2 \rightarrow FeS + H_2S \quad (R4)$$

In our study, the reaction (R1) can be disregarded because of the vacuum environment. Furthermore, the thermal reactions (R2) and (R3) could not have taken place because the estimated surface temperature (≤310 K) is far too low to drive any of them. Concerning COS, Hong and Fegley[89] reported that the only source of COS below 612 °C is the oxidation of S_2 by CO, thus discarding possible reactions of FeS_2 with adsorbed CO and/or CO_2.

Finally, the reaction of pyrite with molecular hydrogen (R4) takes place on surface sulfur anions situating on active points or grain boundaries and having the requisite activation energy of 125 kJ mol^{-1}.[68] Thomas *et al.*[94] suggested that R4 is a free-radical process that starts with the decomposition of FeS_2 and the formation of active sulfur centres, followed by the dissociation of H_2 and the formation of H_2S. It was also reported that the most chemically active centres on pyrite surface are the bridging sulfur atoms and disulfide species.[12,90] Our findings suggest that in tribochemical reactions, like in thermally driven reactions, S^{2-} could be the precursor of the most emitted gases,[94] although the driving forces and the mechanistic pathway may be radically different. This conclusion is based on the observation that the sulfur in the emitted gases was generally in a reduced form (COS, H_2S, and CS_2) while oxidized (SO_2) and/or dimer elemental (S_2) sulfur was at a trace level.

Our findings that the composition of emitted gases depends on the elemental composition of the mechanically activated material suggest that solid-state chemical reactions are the underlying cause of gas emission. For example, the thin film had an oxygen concentration of at least 3.7 at%, and oxygen-containing gases dominated among the triboemitted gases (see Fig. 13). On the other hand, mineral pyrite had only a thin topmost surface layer with oxygen, and the emitted gases were predominantly hydrogen-containing molecules, such as hydrogen and hydrocarbons. Furthermore, the much larger ratio of CH_4/H_2S in mineral pyrite compared to the thin film can be attributed to the higher concentration of carbon in the former. The formation of COS and S_2, which were tightly correlate, is likely due to the breaking of bonds between a surface sulphur atom and the neighbouring matrix atoms. The molecule of carbonyl sulfide has a linear structure, in which carbon is bonded to both oxygen and sulfur. Therefore, it can be

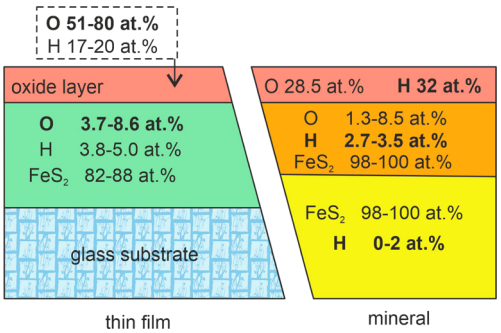

Fig. 13 Schematic structure of the elemental composition of the thin film and mineral pyrite.

Open Access Article. Published on 11 March 2024. Downloaded on 2/11/2026 9:14:28 AM. This article is licensed under a Creative Commons Attribution 3.0 Unported Licence.

formed through the detachment of a sulfur atom, to which CO is adsorbed. Theoretical analysis[95] revealed rich chemistry between COS and CS_2, which can result from shear-induced reactions between adsorbed CO, SO and CS groups. One of the most favourable reactions between two COS molecules leads to the atom rearrangement to form CO_2 and CS_2 molecules with the activation barrier below 65 kcal mol^{-1} at room temperature.[95] In industrial processes such as the thermal step of the modified Claus process, CS_2 can also be formed in the reaction of methane with disulfide or hydrogen sulfide at high temperatures.[96] In our case, the reaction of adsorbed alkyl groups with activated sulfur or disulfide sites is not likely because of weak correlation between CS_2 and both H_2S and H_2. Alternative pathways not involving liberation of hydrogen-containing gases probably should exist.

The H_2S emission could be tentatively assigned to the reaction between lattice hydrogen atoms or protons and sulfur active sites. The presence of hydrogen inclusions in both thin film and mineral pyrite is not surprising as its diffusivity in FeS_2 is as high[97] as 3.5×10^{-4} cm^2 s^{-1} which is 2–4 orders of magnitude larger than in transition metals.

The emission of CO_2 may be due to the decomposition of carbonates, whose presence is evidenced by XPS. The emission of CO_2 usually accompanies fracture or abrasion of alkali earth carbonates,[35] and it is linked to the non-thermal processes such as localized decomposition of carbonates during the relaxation of reversible plastic deformation.[98] The emission of carbon monoxide is likely due to the breaking of C–Fe or C–S bonds between the adsorbed CO and FeS_2. Du *et al.*[99] found that carbon monoxide is strongly bonded to both Fe and S sites, though the former is energetically more favoured, with the predicted binding energies of 140.8 kJ mol^{-1} and 120.8 kJ mol^{-1}, respectively. It is noteworthy that in both cases CO is bonded by the carbon side. The emission of alkanes can stem from the C1 and C2 alkane groups adsorbed on S centres of FeS_2 as shown by the ESD analysis. It likely occurs through a mechanism that was proposed for the emission of alkanes from hydrogenated amorphous carbon,[30,46] and which involves the following two steps:

- formation of the alkyl radical due to breaking of the C–S bond between an adsorbed alkyl group and surface sulfur, and
- the abstraction of hydrogen by an alkyl radical from the environment.

Furthermore, quick response of gas emission to both the beginning and the end of mechanical solicitation in all behaviour modes highlights that emission was predominantly controlled by fast processes.[38] This contrasts the data obtained for metals and hydrides, which usually demonstrate retarded or trail emission due to a significant (up to 20%) contribution from slow processes such as diffusion and migration.[29,100,101] Fast emission kinetics reduces the constraints for processing the gas emission data and facilitates deconvolution of the mass-spectrometry time series into the evolution of mechanochemical activation and the progression of chemical reactions.[33,102] From this perspective, the overall trends of modes β and δ can be put down to the specific chemical reactions rather than to the variations in intensity of mechanochemical activation. More specifically, they can be related to the availability of the precursors of gas molecules along the test.

Another sensible argument supporting the hypothesis of precursors concentration-dependent emission dynamics relies on the presence of the RTEEs in mode β and their absence in mode δ. The RTEEs occur as a result of the material structural degradation such as generation and accumulation of defects, adhesive and cohesive failure, plastic flow, cracking, spalling, formation of debris, their fragmentation at the mechanical interface and so on. These processes may intensify emission of occluded and dissolved gases as well as trigger tribochemical reactions involving the precursors in the mechanically activated volumes and on the new-formed surfaces. Therefore, RTEEs are usually manifested when the sources of gases or their precursors are situated in the material bulk.

To explore the validity of the hypothesis of precursor concentration-controlled gas emission we modelled the general trends of gas emission for various gases using the empirical model of gas triboemission.[33,68,88,101] The model assumes that the instantaneous emission flux of a given gas is a superposition of elemental fluxes from small local volumes of material that have been deformed from the commencement of mechanical action:

$$Q(t) = R(t) \times q_e(t), \quad (1)$$

where R is the rate at which the deformed volume increases, q_e is the gas emission function from the elemental volume of material. The model assumes that the large part of gas emission occurs during the initial deformation of a certain volume of material, while the contribution to the gas flow from the subsequent deformation cycles of this volume can be neglected. The function q_e depends on the concentrations of gases or precursors in the local volume. Bearing in mind that the concentrations are unevenly distributed in depth, we can consider gas flows independently from n thin layers along z. The thickness of the layer, Δz, should be sufficiently small so that the concentrations of gases or precursors in each layer can be considered constant. Then, expression (1) can be transformed as follows:

$$Q(t) = \sum_{i=1}^{n} R_i(t) \times q_{e,i}(t). \quad (2)$$

Function $R_i(t)$ can be determined from the evolution of geometry of MAZ shown in Fig. 11. The approximate analytic expression was derived assuming that the cross-section profile of the MAZ can be fitted by a circular function of radius R_b. It describes the increment of the volume of MAZ in i-th layer, when the total depth of the MAZ increases from b to $b + \Delta b$:

$$R_i|_b = \frac{2l}{\Delta b}\frac{db}{dt}\int_{z_i}^{z_i+\Delta z}\left[\sqrt{{R_b}^2 - (z + R_b - b - \Delta b)^2} - \sqrt{{R_b}^2 - (z + R_b - b)^2}\right]dz, \quad (3)$$

© 2024 The Author(s). Published by the Royal Society of Chemistry

Open Access Article. Published on 11 March 2024. Downloaded on 2/11/2026 9:14:28 AM.
This article is licensed under a Creative Commons Attribution 3.0 Unported Licence.

where db/dt is the rate of increase of the total MAZ depth, which can be determined by differentiation of the plot in Fig. 11, and l is the length of the MAZ along y.

Expression (3) has the following solution:

$$R_i|_b = \frac{l}{\Delta b}\frac{db}{dt}R_b{}^2\Big[\arcsin(C_1) - \arcsin(C_2) - \arcsin(C_3) + \arcsin(C_4) + \frac{1}{2}(\sin(2\arcsin(C_1)) - \sin(2\arcsin(C_2)) - \sin(2\arcsin(C_3)) + \sin(2\arcsin(C_4)))\Big]. \quad (4)$$

where

$$C_1 = 1 - \frac{b - z_i + \Delta z + \Delta b}{R_b}$$

$$C_2 = 1 - \frac{b - z_i + \Delta z}{R_b}$$

$$C_3 = 1 - \frac{b - z_i + \Delta b}{R_b}$$

$$C_4 = 1 - \frac{b - z_i}{R_b}$$

The plots of (4) as function of z for three values of b are presented in Fig. 14. With the increase of b, the graphs shift to the higher z, while the contribution of the topmost layers (at low z) to the total increase of the deformed volume gradually decreases as shown by an arrow in Fig. 14.

As a rough and ready approximation, the function q_e can be assumed constant in time, *e.g.* in the form of a square peak, and proportional to the concentration of gases or precursors in the solid, C_p:

$$q_e(Z) = k_p C_p(Z), \quad (5)$$

where k_p is the coefficient depending on the type of gas, and $C_p(z)$ is the distribution of element concentration obtained by ERDA and RBS. Then, the general trends of gas emission time series were obtained using (2) and are presented in Fig. 15. The rates of H^- and O^-containing gases were determined using concentration profiles of these elements in the thin film.

The model results correlate well with the experimental time series. The O-containing gases showed a trend corresponding to mode β, while the H-containing gases showed a similar trend to mode δ, which is typical for H_2S (Fig. 8). Although in comparison with the experiment, the actual model predicts a slower rise in the emission rate at the beginning of mechanical action, due to omission of the wear intensification at the running-in stage (region I), there is a good match between model and experiment during steady wear (regions II and III). At higher values of n, (region IV) the model slightly deviates upwards. This may be due to a rigid substrate, which could slow the propagation of wear, an effect that was not considered in the model. Notably, the model predicts about three-fold larger emission rate for H-containing gases, in accordance with experiment.

Finally, the formation of Fe_2O_3 in wear debris, as observed by Raman spectrometry, is likely due to oxidation of Fe and FeS_x (which can form as a result of tribochemical decomposition of pyrite) in atmospheric air after the samples are removed from vacuum rather than direct pyrite oxidation in R1 or similar reaction. This is supported by the fact that sulfur dioxide was at a trace level.

From the perspective of mechanochemistry, the driving forces of tribochemical gas emission can be linked to stress, strain or secondary physico-chemical activation processes such as the emission of charged particles, luminescence, the generation and motion of active sites and defects in a crystalline structure, and so on, though the specific mechanism governing tribochemical decomposition of FeS_2 is not clear yet.[14,38,103–106] Literature provides evidence that stress or strain exerted by

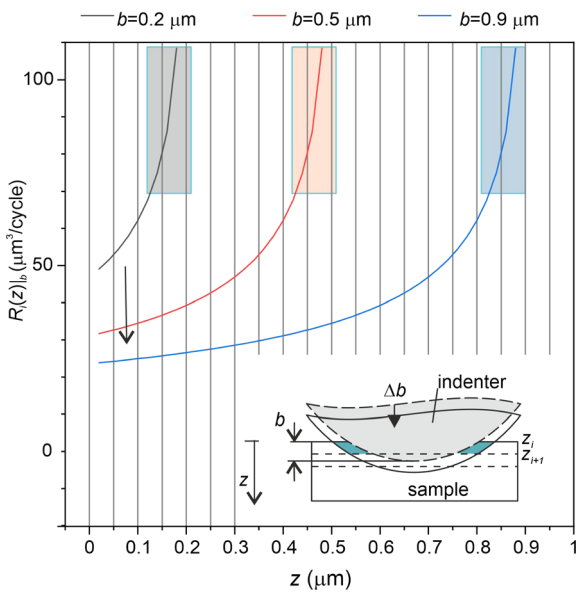

Fig. 14 Function of the rate of increase of the volume of MAZ at different values of z and b. The rectangles denote the ranges of z, where the major increment of the deformed volume takes place. With the increase in b both absolute and relative contributions of the topmost layers to the total increase of deformed volume decreases.

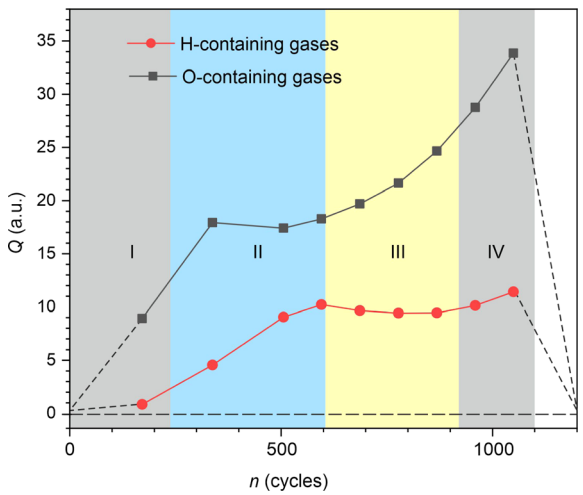

Fig. 15 Predicted trends of emission rates for H- and O-containing gases according to the developed model.

Open Access Article. Published on 11 March 2024. Downloaded on 2/11/2026 9:14:28 AM. This article is licensed under a Creative Commons Attribution 3.0 Unported Licence.

mechanical action can directly couple to the energy landscape of a chemical reaction or can modify it locally, thus reducing potential barriers.[23,107,108]

Conclusions

The analysis of gas emission from thin-film and mineral pyrite subjected to mechanical solicitation was used to elucidate the mechanisms of tribochemical pyrite decomposition. Firstly, a stark difference between the species detected by thermal and mechanical decomposition is highlighted, revealing distinct reaction pathways. While thermal decomposition and oxidation predominantly yield S_2 gas and SO_2, respectively, tribochemical action triggers a richer chemistry, generating two main classes of species: carbon-containing species, including both carbon oxides and hydrocarbons, and sulfur-containing species, such as dihydrogen sulfide, carbonyl sulfide, and carbon disulfide. Notably, carbon and hydrogen, present as inclusions in both thin-film and mineral samples, play a crucial role in tribochemical processes. This finding aligns with the observations of certain chemical affinity between iron pyrite and carbon in both technology and biology.

The gas emission from tribochemically decomposed pyrite was attributed to solid-state chemical reactions, with the kinetics being governed by the precursor concentrations. H-containing gases, including dihydrogen, hydrogen sulfide, and alkanes, were predominant in the emission from H-rich mineral pyrite, while O-containing gases, such as carbon monoxide and dioxide, and carbonyl sulfide, dominated in the emission from O-rich thin-film samples. Notably, sulfur in the emitted gases was primarily in its reduced form, suggesting that redox reactions were not the primary mechanism driving the triboemission process. Overall, these findings support the hypothesis that tribochemical processes in pyrite involve bond switching and reorientation between neighbouring atoms and/or ions under applied stress and shear. This can include radical reactions initiated by the formation of active sulfur centres due to stress-induced bond breaking at disulfide centres. The temperature increase due to frictional heating was found by far insufficient to drive any thermal decomposition or oxidation reaction.

Data availability

Data for this paper is available at the DIGITAL.CSIC, the instutitional repository of the Spanish National Research Council at DOI: **https://doi.org/10.20350/digitalCSIC/15703**.

Author contributions

Conceptualization and methodology: R. N., J. R. A., and E. M. C.; investigation: all; writing – original draft: R. N.; writing – review and editing: all.

Conflicts of interest

There are no conflicts to declare.

Acknowledgements

Authors thank to F. Moreno for his technical assistance. This work was supported by the Ministry of Science and Innovation of Spain (grants PID2019-111063RB-I00, PID2020-112770RB-C22, PID2020-117573GB-I00, RTI2018-099794-B-I00, PID2021-126098OB-I00, and TED2021-129950B-I00). We acknowledge the service from the MiNa Laboratory at IMN and funding from Madrid Community (project S2018/NMT-4291 TEC2SPACE), Ministry of Science and Innovation of Spain (project CSIC13-4E-1794) and EU (ERFD, ESF) The authors acknowledge the support from The Centre for Micro Analysis of Materials (CMAM)—Autonomous University of Madrid, for the beam time proposal (Analysis of surface elemental transformations induced by mechanochemical reactions with metal sulfides) with code STD-022/23, and its technical staff for their contribution to the operation of the accelerator.

Notes and references

1 E. I. Stiefel, in *Transition Metal Sulfur Chemistry*, American Chemical Society, 1996, vol. 653, ch. 1, pp. 2–38.
2 H.-B. Wang, J.-Q. Wang, R. Zhang, C.-Q. Cheng, K.-W. Qiu, Y.-j. Yang, J. Mao, H. Liu, M. Du, C.-K. Dong and X.-W. Du, *ACS Catal.*, 2020, **10**, 4914–4921.
3 J. Gonzalez-Estrella, S. Gallagher, R. Sierra-Alvarez and J. A. Field, *Sci. Total Environ.*, 2016, **548–549**, 380–389.
4 G. Lee and M. Kang, *Curr. Appl. Phys.*, 2013, **13**, 1482–1489.
5 I. J. Ferrer and C. Sánchez, *Solid State Commun.*, 1992, **81**, 371–374.
6 S. Venkateshalu, P. Goban Kumar, P. Kollu, S. K. Jeong and A. N. Grace, *Electrochim. Acta*, 2018, **290**, 378–389.
7 M. V. Morales-Gallardo, A. M. Ayala, M. Pal, M. A. Cortes Jacome, J. A. Toledo Antonio and N. R. Mathews, *Chem. Phys. Lett.*, 2016, **660**, 93–98.
8 A. K. Raturi, S. Waita, B. Aduda and T. Nyangonda, *Renewable Energy*, 2000, **20**, 37–43.
9 M. Walter, T. Zünd and M. V. Kovalenko, *Nanoscale*, 2015, **7**, 9158–9163.
10 M. G. Vladimirov, Y. F. Ryzhkov, V. A. Alekseev, V. A. Bogdanovskaya, V. A. Otroshchenko and M. S. Kritsky, *Orig. Life Evol. Biosph.*, 2004, **34**, 347–360.
11 N. Moslemzadeh, M. Tamara, R. Raval, D. Prior and M. R. Preston, *Surf. Interface Anal.*, 2009, **41**, 1–5.
12 M. Sanchez-Arenillas, S. Galvez-Martinez and E. Mateo-Marti, *Appl. Surf. Sci.*, 2017, **414**, 303–312.
13 M. Adhikari, A. Singh, E. Echeverria, D. N. McIlroy and Y. Vasquez, *ACS Omega*, 2020, **5**, 14104–14110.
14 J.-R. Ares, R. Nevshupa, E. Muñoz-Cortés, C. Sánchez, F. Leardini, I.-J. Ferrer, V. Minh Huy Tran, F. Aguey-Zinsou and J.-F. Fernández, *ChemPhysChem*, 2019, **20**, 1248–1262.
15 L. Jing, Y. Xu, M. Xie, Z. Li, C. Wu, H. Zhao, J. Wang, H. Wang, Y. Yan, N. Zhong, H. Li and J. Hu, *Nano Energy*, 2023, **112**, 108508.
16 B. N. Akhgar and P. Pourghahramani, *Hydrometallurgy*, 2015, **153**, 83–87.

© 2024 The Author(s). Published by the Royal Society of Chemistry

Open Access Article. Published on 11 March 2024. Downloaded on 2/11/2026 9:14:28 AM. This article is licensed under a Creative Commons Attribution 3.0 Unported Licence.

17 P. Pourghahramani and B. N. Akhgar, *Int. J. Miner. Process.*, 2015, **134**, 23–28.
18 A. E. M. Beedle, M. Mora, C. T. Davis, A. P. Snijders, G. Stirnemann and S. Garcia-Manyes, *Nat. Commun.*, 2018, **9**, 3155.
19 P. Balaz, *Mechanochemistry in Nanoscience and Minerals Engineering*, Springer, Berlin, Heidelberg, 2008.
20 L. Takacs, *Chem. Soc. Rev.*, 2013, **42**, 7649–7659.
21 V. V. Boldyrev, *Russ. Chem. Rev.*, 2006, **75**, 177–190.
22 W. G. Sawyer and K. J. Wahl, *MRS Bull.*, 2008, **33**, 1145–1150.
23 H. L. Adams, M. T. Garvey, U. S. Ramasamy, Z. Ye, A. Martini and W. T. Tysoe, *J. Phys. Chem. C*, 2015, **119**, 7115–7123.
24 R. A. Nevchoupa, J. L. De Segovia and E. A. Deulin, *Vacuum*, 1999, **52**, 73–81.
25 R. A. Nevshupa, M. Conte, A. Igartua, E. Roman and J. Luis de Segovia, *Tribol. Int.*, 2015, **86**, 28–35.
26 K. Takiwatari, M. Suzuki, K. Kobayashi and H. Nanao, *Tribology Online*, 2022, **17**, 239–245.
27 S. Mori, T. Kawada and W. C. Xu, *Appl. Surf. Sci.*, 1997, **108**, 391–397.
28 A. Boscoboinik, D. Olson, H. Adams, N. Hopper and W. T. Tysoe, *Chem. Commun.*, 2020, **56**, 7730–7733.
29 R. A. Nevshupa and J. L. de Segovia, *Vacuum*, 2002, **64**, 425–430.
30 A. Rusanov, J. Fontaine, J. M. Martin, T. L. Mogne and R. Nevshupa, *J. Phys.: Conf. Ser.*, 2008, **100**, 082050.
31 J.-M. Martin, M.-I. D. B. Bouchet, C. Matta, Q. Zhang, W. A. Goddard, S. Okuda and T. Sagawa, *J. Phys. Chem. C*, 2010, **114**, 5003–5011.
32 E. A. Varentsov and Y. A. Khrustalev, *Russ. Chem. Rev.*, 1995, **64**, 783–797.
33 R. Nevshupa, J. Ramon Ares, J. Francisco Fernandez, A. del Campo and E. Roman, *J. Phys. Chem. Lett.*, 2015, **6**, 2780–2785.
34 M. G. Aylmore and F. J. Lincoln, *J. Alloys Compd.*, 2000, **309**, 61–74.
35 F. Urakaev, *Phys. Chem. Miner.*, 2007, **34**, 351–361.
36 P. G. Fox and J. Soria-Ruiz, *Proc. R. Soc. A*, 1970, **317**, 79–90.
37 M.-W. Kim, S. C. Langford and J. T. Dickinson, *J. Appl. Phys.*, 2003, **93**, 1819–1825.
38 E. Muñoz-Cortés, O. L. Ibryaeva, M. Manso Silvan, B. Zabala, E. Flores, A. Gutierrez, J. R. Ares and R. Nevshupa, *Phys. Chem. Chem. Phys.*, 2023, **25**, 494–508.
39 C. de las Heras, I. J. Ferrer and C. Sánchez, *J. Appl. Phys.*, 1993, **74**, 4551–4556.
40 W. C. Oliver and G. M. Pharr, *J. Mater. Res.*, 2011, **19**, 3–20.
41 N. Benito and C. Palacio, *Appl. Surf. Sci.*, 2015, **351**, 753–759.
42 K. J. Andersson, H. Ogasawara, D. Nordlund, G. E. Brown and A. Nilsson, *J. Phys. Chem. C*, 2014, **118**, 21896–21903.
43 J. A. Leiro, S. Granroth and K. Laajalehto, *XPS Study of the Sulphur 2p Spectra of Pyrite*, 2003.
44 E. M. Williams and J. L. de Segovia, *Vacuum*, 1989, **39**, 633–642.
45 A. Redondo-Cubero, M. J. G. Borge, N. Gordillo, P. C. Gutiérrez, J. Olivares, R. Pérez Casero and M. D. Ynsa, *Eur. Phys. J. Plus*, 2021, **136**, 175.
46 A. Rusanov, R. Nevshupa, J. Fontaine, J.-M. Martin, T. Le Mogne, V. Elinson, A. Lyamin and E. Roman, *Carbon*, 2015, **81**, 788–799.
47 M. Mahrova, M. Conte, E. Roman and R. Nevshupa, *J. Phys. Chem. C*, 2014, **118**, 22544–22552.
48 R. Nevshupa, M. Conte, S. Guerra and E. Roman, *Lubricants*, 2017, **5**, 27.
49 J. R. Ares, A. Pascual, I. J. Ferrer and C. Sánchez, *Thin Solid Films*, 2005, **480–481**, 477–481.
50 C. Morales, E. Flores, S. Yoda, M. A. Niño, D. Martín y Marero, L. Soriano, J. Rojo, J. R. Ares, I. J. Ferrer and C. Sánchez, *Appl. Surf. Sci.*, 2019, **492**, 651–660.
51 V. P. Evangelou, *Pyrite Oxidation and Its Control*, CRC Press, Boca Raton, 1995.
52 I. Uhlig, R. Szargan, H. W. Nesbitt and K. Laajalehto, *Appl. Surf. Sci.*, 2001, **179**, 222–229.
53 H. W. Nesbitt, G. M. Bancroft, A. R. Pratt and M. J. Scaini, *Am. Mineral.*, 1998, **83**, 1067.
54 H. W. Nesbitt, M. Scaini, H. Höchst, G. M. Bancroft, A. G. Schaufuss and R. Szargan, *Am. Mineral.*, 2000, **85**, 850–857.
55 S. Xu, M. Zanin, W. Skinner and S. Brito e Abreu, *Miner. Eng.*, 2021, **170**, 106992.
56 G. Ruano, F. Pomiro and J. Ferrón, *Surf. Sci.*, 2018, **667**, 138–147.
57 H. W. Nesbitt and I. J. Muir, *Geochim. Cosmochim. Acta*, 1994, **58**, 4667–4679.
58 A. G. Schaufuß, H. W. Nesbitt, I. Kartio, K. Laajalehto, G. M. Bancroft and R. Szargan, *J. Electron Spectrosc. Relat. Phenom.*, 1998, **96**, 69–82.
59 J. L. De Segovia, *Vacuum*, 1996, **47**, 333–340.
60 S. L. Bennett, C. L. Greenwood, E. M. Williams and J. L. de Segovia, *Surf. Sci.*, 1991, **251–252**, 857–860.
61 R. Kumar, *Int. J. Mass Spectrom.*, 2011, **303**, 69–72.
62 J. Aguilar-Santillan, *Acta Mater.*, 2008, **56**, 2476–2487.
63 R. S. O. Ahmadov, Microtextural, elastic and transport properties of source rocks, PhD thesis, submitted to the Department of Geophysics of Stanford University., Stanford University, 2011.
64 T. T. Rao and D. B. Sirdeshmukh, *Cryst. Res. Technol.*, 1994, **29**, K112–K114.
65 K. H. Kissinger, *J. Res. Natl. Bur. Stand.*, 1957, **57**, 217–222.
66 J. L. Falconer and R. J. Madix, *Surf. Sci.*, 1975, **48**, 393–405.
67 F.-q. Yang, C. Wu, Y. Cui and G. Lu, *Trans. Nonferrous Met. Soc. China*, 2011, **21**, 395–401.
68 G.-M. Schwab and J. Philinis, *J. Am. Chem. Soc.*, 1947, **69**, 2588–2596.
69 V. S. Udintseva and G. I. Chufarov, *Zh. Prikl. Khim.*, 1941, **14**, 3.
70 G. Hu, K. Dam-Johansen, S. Wedel and J. P. Hansen, *Prog. Energy Combust. Sci.*, 2006, **32**, 295–314.
71 N. Boyabat, A. K. Özer, S. Bayrakçeken and M. Ş. Gülaboğlu, *Fuel Process. Technol.*, 2004, **85**, 179–188.
72 R. Nevshupa, J. Caro, A. Arratibel, R. Bonet, A. Rusanov, J. R. Ares and E. Roman, *Tribol. Int.*, 2019, **129**, 177–190.
73 P. Bradt, F. Mohler and V. H. Dibeler, *J. Res. Natl. Bur. Stand.*, 1957, **57**, 223–225.

Open Access Article. Published on 11 March 2024. Downloaded on 2/11/2026 9:14:28 AM.
This article is licensed under a Creative Commons Attribution 3.0 Unported Licence.

74 J. Farquhar, in *Encyclopedia of Geochemistry: A Comprehensive Reference Source on the Chemistry of the Earth*, ed. W. M. White, Springer International Publishing, Cham, 2017, pp. 1–8, DOI: 10.1007/978-3-319-39193-9_74-1.
75 H. Vogt, T. Chattopadhyay and H. J. Stolz, *J. Phys. Chem. Solids*, 1983, **44**, 869–873.
76 C. Sourisseau, R. Cavagnat and M. Fouassier, *J. Phys. Chem. Solids*, 1991, **52**, 537–544.
77 S. N. White, *Chem. Geol.*, 2009, **259**, 240–252.
78 C. Sánchez, E. Flores, M. Barawi, J. M. Clamagirand, J. R. Ares and I. J. Ferrer, *Solid State Commun.*, 2016, **230**, 20–24.
79 J. C. Jaeger, *J. Proc. R. Soc. N. S. W.*, 1941, **76**, 203–224.
80 A. A. Yevtushenko, E. G. Ivanyk and O. M. Ukhanska, *Tribol. Int.*, 1997, **30**, 209–214.
81 J. E. Jakes, C. R. Frihart, J. F. Beecher, R. J. Moon, P. J. Resto, Z. H. Melgarejo, O. M. Suárez, H. Baumgart, A. A. Elmustafa and D. S. Stone, *J. Mater. Res.*, 2009, **24**, 1016–1031.
82 T. Fujii, F. M. F. de Groot, G. A. Sawatzky, F. C. Voogt, T. Hibma and K. Okada, *Phys. Rev. B*, 1999, **59**, 3195–3202.
83 F. Huang, L.-Q. Zhang, B.-J. Yi, Z.-J. Xia and C.-G. Zheng, *Fuel Process. Technol.*, 2015, **138**, 814–824.
84 C. Baudín, in *Encyclopedia of Materials: Technical Ceramics and Glasses*, ed. M. Pomeroy, Elsevier, Oxford, 2021, pp. 25–46, DOI: 10.1016/B978-0-12-818542-1.00028-X.
85 M. Asmani, C. Kermel, A. Leriche and M. Ourak, *J. Eur. Ceram. Soc.*, 2001, **21**, 1081–1086.
86 M. Kobayashi, T. Goto, T. Aoba and H. Miura, *Mater. Charact.*, 2019, **154**, 424–436.
87 H. Xu, X. Guo, L. A. Seaman, A. J. Harrison, S. J. Obrey and K. Page, *J. Mater. Res.*, 2019, **34**, 3243–3253.
88 P. Auerkary, *Mechanical and physical properties of engineering Alumina ceramics*, Technical notes, Julkaisija – Utgivare, Technical research center of Finland, Espoo, 1996.
89 Y. Hong and B. Fegley Jr, *Ber. Bunsenges. Phys. Chem.*, 1997, **101**, 1870–1881.
90 J. Liu, T. Yang, Q. Peng, Y. Yang, Y.-W. Li and X.-D. Wen, *Appl. Surf. Sci.*, 2021, **537**, 147900.
91 Z. Zheng, Y. You, J. Guo, G. Li, Z. You and X. Lv, *ACS Omega*, 2022, **7**, 29116–29124.
92 C. Tian, Y. Rao, G. Su, T. Huang and C. Xiang, *J. Chem.*, 2022, **2022**, 8160007.
93 J. M. Lambert, G. Simkovich and P. L. Walker, *Metall. Mater. Trans. B*, 1998, **29**, 385–396.
94 M. G. Thomas, T. D. Padrick, F. V. Stohl and H. P. Stephens, *Fuel*, 1982, **61**, 761–764.
95 T. Li, J. Li, H. Zhang, S. Yang, J. Wang and J. Xiao, *Combust. Flame*, 2020, **221**, 311–325.
96 K. Karan and L. A. Behie, *Ind. Eng. Chem. Res.*, 2004, **43**, 3304–3313.
97 S. M. Wilhelm, J. Vera and N. Hackerman, *J. Electrochem. Soc.*, 1983, **130**, 2129–2132.
98 J. T. Dickinson, L. C. Jensen, S. C. Langford, P. E. Rosenberg and D. L. Blanchard, *Phys. Chem. Miner.*, 1991, **18**, 320–325.
99 Y. Du, W. Chen, Y. Zhang and X. Guo, *J. Nat. Gas Chem.*, 2011, **20**, 60–64.
100 M. R. Louthan, G. R. Caskey, J. A. Donovan and D. E. Rawl, *Mater. Sci. Eng.*, 1972, **10**, 357–368.
101 R. Nevshupa, K. Cruz, I. Martinez, S. Ramos, I. Llorente and E. Roman, *Tribol. Int.*, 2016, **97**, 360–370.
102 R. A. Nevshupa, E. Roman and J. L. de Segovia, *Int. J. Mater. Prod. Technol.*, 2010, **38**, 57–65.
103 R. A. Nevshupa, J. L. de Segovia and E. Roman, *Vacuum*, 2005, **80**, 241–246.
104 R. A. Nevshupa, *J. Frict. Wear*, 2009, **30**, 118–126.
105 A. Rusanov, R. Nevshupa, J.-M. Martin, M. Á. Garrido and E. Roman, *Diamond Relat. Mater.*, 2015, **55**, 32–40.
106 R. A. Nevshupa, *J. Phys. D: Appl. Phys.*, 2013, **46**, 185501.
107 T. Kuwahara, Y. Long, M.-I. De Barros Bouchet, J. M. Martin, G. Moras and M. Moseler, *Coatings*, 2021, **11**, 1069.
108 J. Ribas-Arino and D. Marx, *Chem. Rev.*, 2012, **112**, 5412–5487.

© 2024 The Author(s). Published by the Royal Society of Chemistry